Title
Terahertz Metasurface Quantum-Cascade VECSELs: Theory and Performance

Journal
IEEE Journal of Selected Topics in Quantum Electronics, 23(6)

ISSN
1077-260X

Authors
Xu, Luyao
Curwen, Christopher A
Chen, Daguan
et al.

Publication Date
2017

DOI
10.1109/jstqe.2017.2693024

Peer reviewed

Terahertz metasurface quantum-cascade VECSELs: theory and performance

Luyao Xu, *Student Member, IEEE*, Christopher A. Curwen, *Student Member, IEEE*, Daguan Chen, John L. Reno, Tatsuo Itoh, *Life Fellow, IEEE*, and Benjamin S. Williams, *Senior Member, IEEE*

***Abstract* — Achieving both high power and high-quality beam pattern has been a longstanding challenge for terahertz quantum-cascade (QC) lasers largely due to their use of sub-wavelength metallic waveguides. Recently, the vertical-external-cavity surface-emitting laser (VECSEL) concept was demonstrated for the first time in the terahertz range and for a QC-laser. This is enabled by the development of an amplifying metasurface reflector capable of coupling incident free-space THz radiation to the QC-laser material such that it is amplified and re-radiated. The THz metasurface QC-VECSEL initiates a new approach for making QC-lasers with high power and excellent beam pattern. Furthermore, the ability to engineer the electromagnetic phase, amplitude, and polarization response of the metasurface enables lasers with new functionality. This article provides an overview of the fundamental theory, design considerations, and recent results for high-performance THz QC-VECSELs.**

***Index Terms*—Quantum cascade laser, VECSEL, terahertz, metasurface, reflectarray**

I. Introduction

Since its invention in 2002 [1], the terahertz (THz) quantum-cascade laser has developed to be a compact semiconductor THz source capable of delivering milliwatt-level power or higher at various frequencies from 1.2 – 5.6 THz [2-6]. In the best devices, the operating temperature has reached 200 K in pulsed mode [7] and 129 K in continuous wave (cw) mode [8]. One longstanding challenge for THz QC-lasers is combining high power output and high-quality beam pattern in one device, which is desired for many applications such as heterodyne spectroscopy [9-11], and real-time imaging [12] (e.g. for biomedical [13, 14], or nondestructive inspection applications) [15, 16]. Although the beam from an edge-emitting THz QC-laser with a sub-wavelength sized metal-metal waveguide is highly divergent [17], significant advances in beam shaping have been demonstrated, including using facet-mounted lenses [18], 3rd-order distributed feedback (DFB) end-fire antenna lasers [19, 20], 2nd-order surface-emitting DFB arrays or a graded photonic heterostructure cavities (GPH) [21, 22], 2D photonic crystal cavity [23], phase-locked laser array through antenna mutual coupling [24], and DFB laser based on antenna-feedback mode [25]. Nonetheless, there still exists considerable room for improvement in achieving high power and high efficiency output combined with an excellent beam.

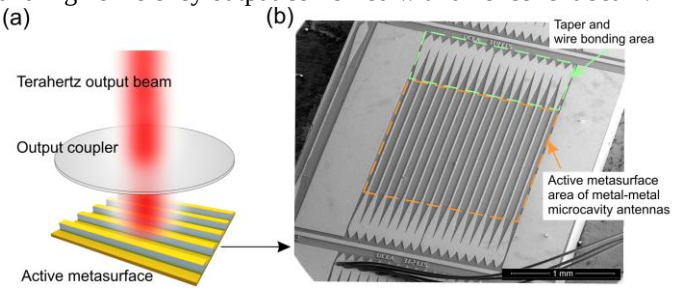

Fig. 1. (a) Schematic of a QC-VECSEL comprised of an active metasurface and an output coupler. (b) SEM image of a fabricated active metasurface with a 1.5-by-1.5 mm^2 active area of metal-metal microcavity antennas ended by taper and wire-bonding area.

The vertical-external-cavity surface-emitting laser (VECSEL) approach has been very successful towards combining high power and high-quality beam pattern for interband semiconductor lasers in the visible and near-infrared range [26-28]. The basic configuration is an optically pumped semiconductor gain medium backed by a distributed Bragg reflector, which forms one or more mirrors in an open optical cavity. Because the cavity can be designed to preferentially support only the fundamental TEM_{00} Gaussian mode, very high beam quality can be obtained without the divergence and astigmatism found in edge emitting semiconductor lasers. Provided the active material is well heat sunk, by increasing the area of the optical pump the power can be scaled up without issues of multi-mode instabilities. However, it had been impossible to implement this approach for QC-lasers due to the "intersubband selection rule" in which the electric field must be polarized perpendicular to the plane of the quantum well to be amplified by QC-material gain. This is incompatible with the natural polarization for surface incident waves in a VECSEL cavity. To address this issue, we developed an active reflectarray metasurface consisting of an array of metallic microcavity antennas loaded with QC gain material; each antenna efficiently couples in THz radiation, amplifies it and

This work was supported in part by the National Science Foundation (NSF) (Grants 1150071, 1407711), and the National Aeronautics and Space Administration (NASA) (Grant NNX16AC73G). This work was performed, in part, at the Center for Integrated Nanotechnologies, an Office of Science User Facility operated for the U.S. Department of Energy (DOE) Office of Science. Sandia National Laboratories is a multi-program laboratory managed and operated by Sandia Corporation, a wholly owned subsidiary of Lockheed Martin Corporation, for the U.S. Department of Energy's National Nuclear Security Administration under contract DE-AC04-94AL85000.

L. Xu, C. A. Curwen, D. Chen, T. Itoh, and B. S. Williams are with the Department of Electrical Engineering, University of California, Los Angeles, CA 90095 USA (e-mail: bswilliams@ucla.edu).

B. S. Williams is also with the California NanoSystems Institute (CNSI), University of California, Los Angeles, CA 90095 USA.

J. L. Reno is with Sandia National Laboratories, Center of Integrated Nanotechnologies, MS 1303, Albuquerque, New Mexico, 87185 USA.

re-radiates into the free space. The amplifying metasurface reflector is then paired with an output coupler to create an external laser cavity. This approach was used to demonstrate the first VECSEL in the terahertz regime, which exhibited lasing in a near-Gaussian beam pattern with considerable power output [29]. A schematic of a QC-VECSEL is shown in Fig. 1(a). This approach is fundamentally different from the previous beam shaping techniques – it is the super mode of the VECSEL cavity, rather than the mode of the individual metallic microcavities on metasurface, that exhibits lasing and shapes the beam to a near-Gaussian profile. The metasurface is deliberately designed to have a low radiative quality factor so that the sub-cavities will not self-oscillate in the absence of an external cavity. Furthermore, since each microcavity also supports a highly confined fundamental waveguide mode, absorbing boundary conditions are placed at the terminations in the form of lossy tapers to suppress self-lasing (see Fig. 1(b)). Compared to conventional THz QC-lasers, the advantage of the VECSEL can be summarized as: (a) the output power is scalable with the active area on the metasurface as more active microcavities contribute stimulated emission to the VECSEL cavity mode, (b) the beam quality is primarily determined by the external cavity, (c) compared to monolithic cavities it is easier to achieve the optimum coupling condition and maximize the output power by choosing the reflectance of the output coupler, (d) the sparse arrangement of the microcavities reduces the power dissipation density for improved cw performance. Of course, these advantages must be balanced against the additional size and complexity of an external cavity.

This paper is organized as follows. In Sec. II, we discuss the design of active metasurface. In Sec III, we lay out a fundamental theory for the basic VECSEL performance. In Sec. IV, we discuss several QC-VECSEL cavity designs. In the Sec. V, we present and discuss several experimental results that demonstrate spectral versatility, variable output-coupling efficiency, high power with high-quality beam pattern achieved from QC-VECSELs.

II. Active Metasurface Design

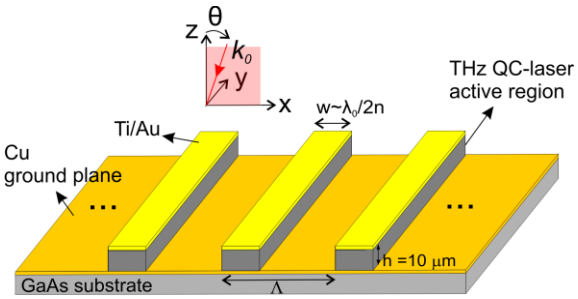

Fig. 2. A schematic of an active metasurface design consisting of a metal-metal microcavity array.

The active metasurface reflector plays a key role in the QC-VECSEL to both provide the gain and constitute the cavity. In the baseline form, the active metasurfaces are composed of a sparse array of identical metal-metal waveguide ridges, a schematic of which is shown in Fig. 2. Each ridge is made up of GaAs/AlGaAs multiple-quantum-well QC-active material (usually 10 μm thick), with metal cladding/contacts directly above and below. Fabrication takes place via a metal-metal thermocompression wafer bonding technique followed by substrate removal via selective wet etching, conventional microfabrication via photolithography, dry etching, and metallization, as is standard for THz QC-lasers [30]. When electrically biased, the material provides a gain described by the bulk material gain coefficient $g(\nu)$. Each element acts as a THz microcavity antenna to couple in incident THz radiation (polarized transverse to the ridge axis), amplify it via stimulated emission, and re-radiate back into free space. Each microcavity resembles an elongated microstrip patch antenna, and is resonant at a wavelength that approximately corresponds to $w \approx \lambda_0/2n$, where n is the refractive index of the QC active material, w is the ridge width, and λ_0 is the free-space wavelength [31-34]. This can be thought of also as the cutoff frequency of the first higher-order lateral mode (TM_{01}) of the metal-metal waveguide. The microcavities are spaced with a period Λ designed to be less than the λ_0 (of intended laser emission), in order to suppress higher-order Bragg diffraction – only zeroth-order (specular) reflection occurs. As we will discuss below, for $\Lambda \ll \lambda_0$ this resonance frequency is predominantly determined by the ridge width w and only slightly affected by the period Λ – however as the period approaches the free-space wavelength, a coupling occurs between the localized resonance and a propagating Bloch surface wave.

Numerical simulation of the metasurface is conducted using a full-wave finite-element electromagnetic solver (COMSOL 5.2), in which a 2-dimensional unit cell of metasurface is modeled with Floquet periodic boundary conditions applied to depict an infinite structure. The Drude model was used to describe the free carrier scattering loss in GaAs/AlGaAs and gold metallization that accounts for the loss in the metasurface (free carrier density used for metal is 5.9×10^{22} cm^{-3} and for active medium is 5×10^{15} cm^{-3}. Drude lifetime used for metal is 39 fs and active medium is 0.5 ps [35, 36]). Fig. 3(a) shows a set of simulated reflectance spectra for a group of metasurfaces with different ridge widths ranging from 11–12.5 μm and a fixed periodicity Λ = 70 μm for two scenarios: passive with g = 0 cm^{-1} and active with g = 30 cm^{-1} in the QC-material. As expected, reducing the width w leads to a higher resonance frequency. Fig. 3(b) shows the reflectance increases with gain for the metasurface with w = 11.5 μm and Λ = 70 μm at its resonance frequency 3.4 THz and two other frequencies above and below the resonance. As shown in Fig. 3(b) the reflectance R_{MS} increases with the gain g; it is useful to fit these numerical results to the relation

$$R_{MS} = R_1 G = e^{\xi(\nu)(g-g_{tr})} \quad . \tag{1}$$

where R_1 is the passive metasurface reflectance at frequency ν, G is the intensity gain, g_{tr} is the transparency gain coefficient needed to balance absorption losses (from the metal and semiconductor), and $\xi(\nu)$ is a fitting coefficient that contains information about the metasurface frequency response and quality factor. Gain is more efficiently coupled to incident radiation when the operation frequency is closer to the

resonance, which is represented by a higher value of $\xi(v)$. The excited microcavity mode has its E-field inside the gain medium predominantly polarized perpendicular to the quantum wells, satisfying the intersubband selection rule. In these simulations, we assumed a frequency-independent gain for the active medium, so that the metasurface response can be analyzed independently of the choice of active material. In reality, the gain will have its own lineshape; the general design goal is to match the metasurface resonance with the peak gain frequency of the gain medium. In practice, this is typically accomplished by first measuring the lasing spectrum of a conventional metal-metal waveguide QC-laser fabricated from the same active material, and then designing the metasurface dimensions around the measured values.

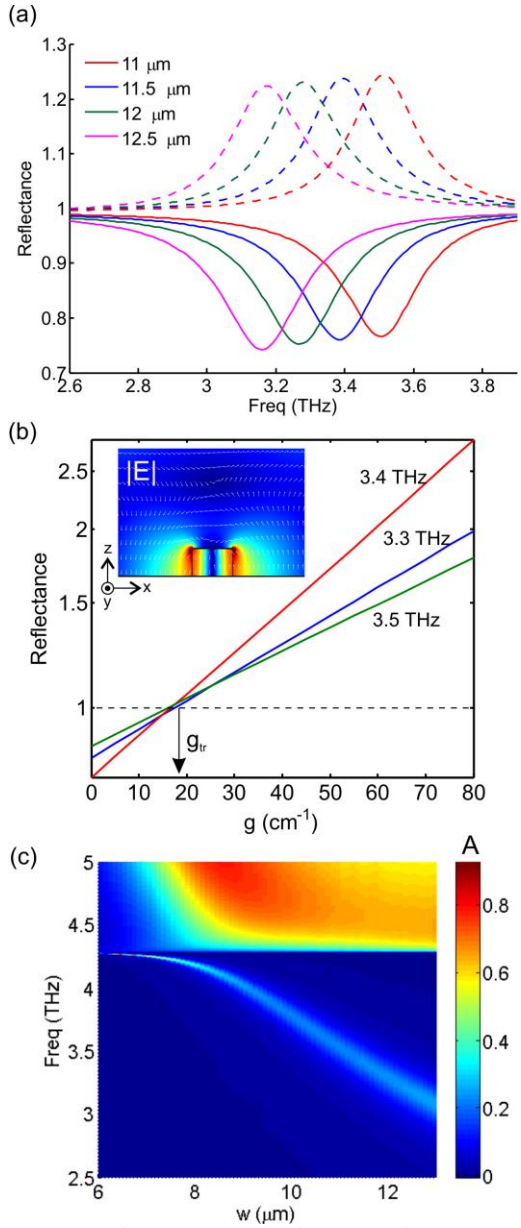

Fig. 3. (a) Simulated reflectance spectra for four metasurfaces with ridge widths varying from 11-12.5 μm and fixed period Λ = 70 μm. The solid lines are results for passive metasurface with g = 0 cm^{-1}, and the dashed lines are for active metasurface with g = 30 cm^{-1}. (b) Simulated reflectance change (plotted in log scale) with medium gain (g) for a metasurface with w = 11.5 μm and Λ = 70 μm at different frequencies. The transparency gain g_{tr} is almost fixed. The inset shows the E-field profile for the excited TM_{01} mode. (c) Colormap of the simulated absorption (A = 1-R_{MS}) spectra for a passive metasurface with ridge width w varied from 6 - 13 μm and period Λ fixed at 70 μm.

It is important to note that despite its resemblance to a grating, the primary mechanism of operation for the metasurface is *not* Bragg-scattering. Rather, each microcavity antenna is locally selfresonant on the unit cell level. This is readily seen in simulated absorption (A = 1-R_{MS}) spectra from a passive metasurface with ridge width w varied in a large range from 6 – 13 μm and period Λ fixed at 70 μm, shown in Fig. 3(c). Two bands are observed in this dispersion map. For a large ridge width (>9 μm), the lowest frequency mode is the localized microcavity resonance; it scales inversely with w, and has a relatively broad bandwidth due to the low radiative quality factor (Q) of the antenna (Q~10–15 in simulation). The higher frequency band at and above ~4.3 THz represents a propagating surface Bloch waves that is coupled to normally incident radiation via Bragg scattering when $\lambda_0 \approx \Lambda$ or $\lambda_0 \leq \Lambda$. The passive reflectance spectra for ridge widths varying from 11 – 12.5 μm in Fig. 3(a) are the line cuts from part of this spectral map, excluding the high frequency region containing Bragg scattering features. However, as the ridge width is reduced, the microcavity mode resonance increases in frequency and hybridizes with the surface Bloch wave mode, which is characterized by an anticrossing feature. This is accompanied by an increase in the radiative Q of the microcavity mode and an increased dependence on Λ of the resonance frequency, a phenomenon which has been observed in a variety of coupled systems [37, 38]. Despite the higher Q of the surface Bloch wave, this mode is undesirable for VECSEL operation, since it is less confined to the active region, and for a finite sized metasurface, is associated with considerable scattering and diffraction losses. Thus, we typically remain in the region of design space where the microcavity mode resonance is clearly distinct from the surface Bloch wave.

A further complication arises due to the fact that a finite sized beam incident upon the metasurface will contain components with non-zero transverse momentum, i.e. obliquely incident components could more easily excite the surface Bloch wave than expected from plane wave simulations [39]. For a non-zero incident angles θ as defined in Fig. 2. this excitation occurs at a frequency lower than the first-order Bragg diffraction (at c/Λ). For example, in one of our early metasurface designs for 2.7–3.0 THz, we chose period Λ = 90 μm (corresponding to c/Λ ~3.33 THz), with the ridge width varied from 11.5–13.5 μm to overlap with the gain peak [29]. The reflectance spectra have been measured using a FTIR spectrometer for these five metasurfaces, nominally at normal incidence (see Fig. 4(a)). First, as expected, resonances are only observed when the incident radiation is polarized transverse to the ridge axis. Second, the spectra clearly show two absorption features, corresponding to the microcavity TM_{01} mode resonance and surface guided mode excitation. As w decreases, the resonance frequency increases. For w = 11.5 μm and 12 μm width designs, the resonances become strongly coupled and an anticrossing is observed. This is consistent with our

experimental observations: VECSEL designs based upon w = 12.5, 13 μm metasurfaces all were observed to lase (see spectra in Fig. 4(a)), while designs with w = 12, 11.5 μm did not lase, despite the fact that the active material was known to have strong gain at those frequencies. A metasurface with w = 13.5 μm did not exhibit lasing likely due to the spectral mismatch between metasurface resonance and the gain medium. The effect of the surface wave is also manifested in reflectance spectrum simulations for a metasurface (w = 12.5 μm, Λ = 90 μm) under plane wave incident from different angles, as seen in Fig. 4(b). Since it is an infinite structure simulation, for normal incidence θ = 0° the localized microcavity resonance is at 3.0 THz, and the first-order Bragg diffraction is observed starting at ~3.33 THz, almost exactly at c/Λ. For θ = 2°, a guided mode is excited at 3.16 THz, which is bound to the metasurface and propagates in the transverse direction, as Fig. 4(d) shows. This is very different from the localized microcavity mode excited at 3 THz (see Fig. 4(e)). The coupling of two modes also narrows and shifts the microcavity mode resonance dips. This impact is increased with a larger incident angle as the guided mode excitation occurs at a lower frequency. The key strategy to suppress the impact of the surface wave is to further reduce the period Λ compared to λ_0 – perhaps more than would be initially expected. As seen in Fig. 4(c), by reducing Λ from 90 to 80 μm, the guided mode excitation is pushed to frequencies much higher than the microcavity resonance, which is therefore slightly affected by oblique incidence. The primary drawback to this strategy is the desire to minimize the fill factor w/Λ to minimize the thermal dissipation per unit metasurface area, which is especially important for THz QC-laser cw performance.

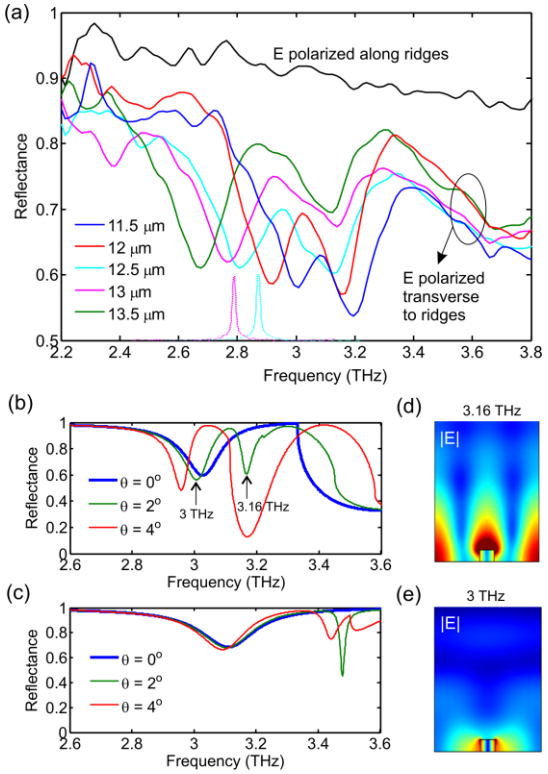

Fig. 4. (a) Measured reflectance spectra for five metasurfaces with ridge widths ranging from 11.5 – 13.5 μm and Λ = 90 μm, with the incident E-field polarized transverse to the ridges. The reference used is a flat gold surface. The black line is the measured with E-field polarized along the ridges. The lasing spectra measured at 77 K for two QC-VECSELs based on w = 12.5, 13 μm metasurfaces are plotted in the corresponding color below the reflectance spectra. (b) Simulated spectra for a metasurface with 12.5 μm ridge width and Λ = 90 μm with a plane wave incident at different incident angles. For 2° incident angle, the excited guided mode at 3.16 THz is shown in (d) and the TM_{01} microcavity mode resonant at 3 THz is plotted in (e). (c) Simulated spectra for a metasurface with 12.5 μm ridge width and 80 μm period with a plane wave incident at different angles.

III. Laser Model for Idealized QC-VECSEL

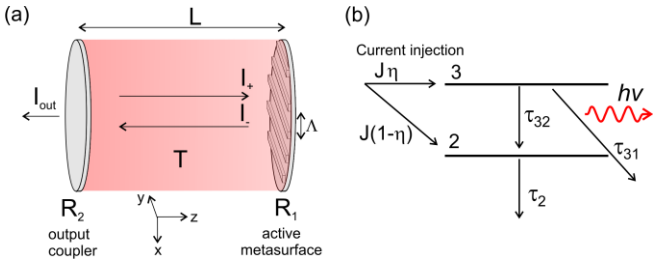

Fig. 5. (a) Schematic of idealized metasurface VECSEL cavity with mode area of A and length L, where the metasurface sub-cavity period is Λ. (b) Three-level model for QC-laser gain medium, where non-radiative relaxation times τ_{32}, τ_{31}, and τ_2 are explicitly shown. Level 1 (injector state) is not explicitly shown.

In this section we derive a basic formalism to describe the threshold condition and slope efficiency for an idealized QC-VECSEL. We consider a cavity as illustrated in Fig. 5(a), constituted between a metasurface reflector of area A with passive reflectance R_1, and an output coupler with reflectance R_2 and transmittance T_2=1-R_2. The incident and reflected circulating intensities are I_+ and I_- respectively, as defined just above the metasurface. We also include a single-pass transmittance T for the propagation over the cavity length L which includes the effect of diffraction loss, atmospheric absorption, and cryostat window transmission. The metasurface produces a uniform power gain $G = e^{\xi g}$, so that its active reflectance is equal to R_1G. The bulk gain coefficient of the active QC-laser material at the cavity mode frequency v is $g=g(v)$. We assume for the moment that the intensity is uniform in the transverse direction, and that the mode area and metasurface area are identical; later we will modify our expression to account for a transverse confinement factor. Using Eq. (1), the threshold gain coefficient g_{th} is obtained by requiring the intensity to be unchanged after one round trip:

$$g_{th} = -\frac{\ln\left(T^2 R_1 R_2\right)}{\xi}. \qquad (2)$$

To go further, we model the QC-laser active material as a 3-level system, as shown in Fig. 5(b). The upper radiative state 3 is pumped using tunneling current injection at a rate of $J\eta/eL_p$, where J is the current density, η is the injection efficiency, e is the fundamental charge, and L_p is the length of one cascade period. The remaining fraction (1-η) of current density is injected into the lower radiative state 2, which is then emptied by some combination of tunneling and electron-phonon scattering. The various non-radiative lifetimes are given by τ_3, τ_{32}, and τ_2. This is a standard treatment for QC-laser systems similar to that given in Refs. [40, 41].

Within the active material, we use a standard expression for the saturated gain coefficient for a homogeneously broadened gain transition:

$$g = \frac{g_0(J)}{1+I_0/I_s} = \frac{(J-J_{leak})\sigma\tau_{eff}}{eL_p}\frac{1}{1+I_0/I_s}, \quad (3)$$

where $g_0(J)$ is the unsaturated gain coefficient, which we assume is proportional to the pump current density J. J_{leak} is an empirical shunt leakage current. The effective upper state lifetime is given by $\tau_{up} = \tau_3(1-\tau_2/\tau_{32})$, and the effective lifetime for population inversion is $\tau_{eff} = \eta\tau_{up} - (1-\eta)\tau_2$, which accounts for a non-unity injection efficiency η. For the case of $\eta = 1$ we see $\tau_{eff} = \tau_{up}$. The circulating intensity within each sub-cavity ridge is I_0, and the saturation intensity is $I_s = h\nu/\sigma(\tau_{up}+\tau_2)$. The stimulated emission cross section at the cavity frequency is $\sigma(\nu)$, such that $g(\nu) = \sigma(\nu)(n_3 - n_2)$, where n_3 and n_2 are the 3D population densities of levels 3 and 2 respectively. Setting the value $g = g_{th}$, we can obtain an expression for the intensity vs. current density:

$$I_0 = \frac{h\nu}{eL_p}\frac{\tau_{eff}}{\tau_2+\tau_{eff}}\frac{(J-J_{th})}{g_{th}}, \quad (4)$$

where the threshold current density is:

$$J_{th} = \frac{g_{th}eL_p}{\sigma\tau_{eff}} + J_{leak}. \quad (5)$$

We now must relate the intensity I_0 inside the microcavity to the open cavity circulating intensities. The field within each of the N microcavities centered at x_i can be well approximated by a standing wave field profile. The field within the cavity of length L can be then be approximated as

$$\mathbf{E} = \underbrace{\hat{x}E_+\psi(x,y)\left(e^{ik_0 z} + r_1\sqrt{G_{th}}e^{-ik_0 z}\right)}_{\text{open cavity}} + \underbrace{\sum_{i=1}^{N}\hat{z}E_0\psi(x,y)\sin\left(\frac{\pi}{w}(x-x_i)\right)}_{\text{inside sub-cavities only}}, \quad (6)$$

where $\hat{x}$ is the unit vector transverse to the microcavity ridges, r_1 is the field reflection coefficient of the metasurface, and $\psi(x,y)$ is a slowly varying transverse modal profile (assumed for now to be unity – i.e. a top-hat beam). Conservation of energy requires

$$A(I_- - I_+) = \frac{dU}{dt} = \frac{\omega_0 U_0}{Q_{abs}}, \quad (7)$$

where U_0 is the electromagnetic energy stored inside the antenna microcavity, ω_0 is resonance frequency, and Q_{abs} represents the nonradiative quality factor of the microcavity that accounts for the absorption loss. We write U_0 based on (6):

$$U_0 = AF\frac{1}{4}\varepsilon_r\varepsilon_0 E_0^{\,2}h, \quad (8)$$

where h is the microcavity height determined by the active material thickness, ε_{r} is the relative permittivity of the active material, and F is the fill factor of biased antenna area over the entire metasurface area ($F = w/\Lambda$ for the metasurface shown in Fig. 2). We further write $Q_{abs} = \frac{\omega_0 n}{(g_{tr}-g)c}$, where transparency gain $g_{tr} = -\xi^{-1}\ln R_1$, and is obtained from numerical simulations such as described in Sec. II. Using the relation $I_- = R_1 G I_+ = c\varepsilon_0 E_-^{\,2}/2$ and combining Eq. (7) and (8), we can define a field enhancement factor M as

$$M = \frac{|E_0|^2}{|E_-|^2} = \frac{2(1-R_1G)}{R_1G(g_{tr}-g)nhF}. \quad (9)$$

The output intensity is written as $I_{out} = (1-R_2)TI_-$. With $I_0 = nc\varepsilon_0 E_0^{\,2}/4$ and $I_+ = c\varepsilon_0 r^2 E_+^{\,2}/2$ we can write the output intensity as:

$$I_{out} = \frac{2(1-R_2)T}{nM}I_0. \quad (10)$$

Substituting Eq. (4) and (9) to Eq. (10), using the laser threshold condition $R_1G_{th} = (R_2T^2)^{-1}$, and multiplying by the metasurface area A, we obtain the total output power as

$$P_{out} = N_p\frac{h\nu}{e}\underbrace{\frac{\tau_{eff}}{\tau_2+\tau_{eff}}}_{\eta_i}\underbrace{\frac{T(1-R_2)\ln(R_2T^2)}{(1-R_2T^2)\ln(R_1R_2T^2)}}_{\eta_{opt}}(I-I_{th}), \quad (11)$$

and

$$I_{th} = AF\left[\frac{eL_p}{\sigma\tau_{eff}}\frac{-\ln(R_1R_2T^2)}{\xi} + J_{leak}\right]. \quad (12)$$

A. *Modal Nonuniformity*

The derivation so far doesn't account for the effects of modal non-uniformity and spatial hole burning. For example, the effect of modal nonuniformity is to reduce the slope efficiency near threshold, as the injected current is effectively wasted in regions with low modal intensity. The effect of spatial hole burning is particularly acute in THz QC-lasers, due to the long length scale of the standing wave (~10 μm) compared to the lateral diffusion lengths of the inverted carrier population (estimated at a few hundred nm). As derived in Ref. [42], this effect results in a nonlinear *P-I* curve, however near threshold a linearized expression can be derived, and included through an additional "uniformity efficiency" factor $\eta_u \leq 1$ into Eq. (11). The slope efficiency near threshold can then be written:

$$\frac{dP}{dI} = N_p\frac{h\nu}{e}\eta_{opt}\eta_i\eta_u. \quad (13)$$

Since the electric field is polarized almost entirely in the z-direction within metal-metal waveguides (see Fig. 3(b) main text), the uniformity factor associated with the microcavity mode can be written as

$$\eta_u = \underbrace{\frac{\left(\int_{act}|E_z|^2\,dA\right)^2}{A_{act}\int_{act}|E_z|^4\,dA}}_{\text{microcavity}}\underbrace{\frac{\left(\int_A|\psi(x,y)|^2\,dA\right)^2}{A\int_A|\psi(x,y)|^4\,dA}}_{\text{cavity mode shape}}. \quad (14)$$

The first factor describes the modal uniformity within each

microcavity, and the second factor describes the uniformity of the slowly varying cavity mode profile incident upon the metasurface. While η_u can be solved exactly from numerical results, for a uniform cavity mode and the sinusoidal dependence of the mode within the microcavity described by Eq. (6), $\eta_u = 2/3$ (very close to the value of 0.65 extracted from a finite element simulation (inset of Fig. 3(b))). If the transverse beam $\psi(x,y)$ within the cavity is not uniform, then η_u will be further reduced. This function is plotted for a Gaussian beam with spot size w_0 on a square metasurface, where only the center circular area of diameter $2a$ is biased. The uniformity is shown in Fig. 6 and suggests that under-filling a metasurface with the beam will cause a significant reduction in output power. Transverse mode confinement factor Γ_t as defined in Eq. (17) in the Appendix is also plotted in Fig. 6, which exhibits a trend opposite to η_u. This suggests a tradeoff between these two factors in the metasurface bias area design.

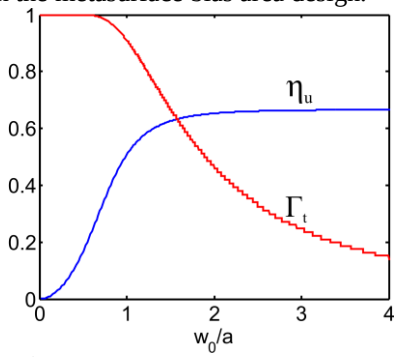

Fig. 6. Uniformity factor η_u according to Eq. (14) and transverse confinement factor Γ_t according to Eq. (17) in the Appendix for Gaussian beam with spot size waist w_0 on a square metasurface where only the center circular area with a diameter of $2a$ is biased.

The effects of modal uniformity and spatial hole burning illustrate one of the largest differences between the metasurface VECSEL and conventional Fabry-Pérot waveguide QC-lasers. While longitudinal spatial hole burning in a semiconductor laser also results in a reduced η_u for any given mode, in a Fabry-Pérot laser multi-mode oscillation "washes-out" the overall field nonuniformity and allows for the most efficient use of the available gain. Hence η_u typically does not appear in most conventional expressions for the slope efficiency. However, in a VECSEL cavity, all of the various longitudinal modes in the external cavity interact with the active material through the same metasurface resonance, and have the same uniformity factor η_u. This may lead to a suppression of multi-mode operation – more work is needed to fully understand this phenomenon. However, we should also point out that this effect may be "engineerable" by designing spectrally and spatially inhomogeneous metasurfaces.

IV. Cavity Design

QC-VECSELs have been demonstrated in a variety of external cavity types. The first demonstrations of QC-VECSELs were made with a gold concave mirror external to the cryostat in conjunction with the active metasurface mounted within to form a hemispherical cavity, as shown in Fig. 7(a) [43]. While the concave mirror provides nearly unity reflection to the cavity, outcoupling is not possible unless a hole is drilled in the mirror. Given that partially transmitting spherical mirrors are not readily available in THz range, we soon turned to using flat output couplers to build plano-plano Fabry-Pérot (FP) cavities by as shown in Fig. 7(b). It is possible to use an off-the-shelf wire grid polarizer as an output coupler [29]. A particular advantage of this approach is that the output coupling efficiency is tunable with the polarizer's orientation, enabled by the polarized response from both the metasurface and the polarizer. This allows optimization of the power "on-the-fly" simply by turning the output coupler to reach the optimum coupling point. However, the polarization eigenstate for the circulating cavity mode is non-trivial, and a function of orientation, which complicates analysis.

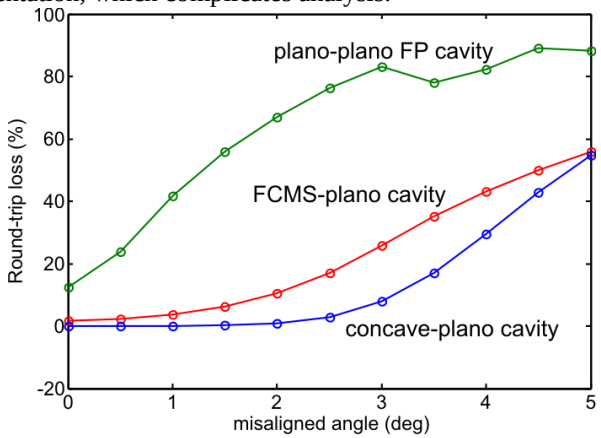

Fig. 8. Calculated round-trip cavity loss induced by beam walk-off due to angular misalignment vs. misaligned angle for three types of cavity: plano-plano Fabry-Pérot cavity, focusing-metasurface (FCMS)-plano near-Gaussian cavity, concave mirror-plano Gaussian cavity. All the other sources of loss are neglected.

Meanwhile, we designed and fabricated a number of THz output couplers (OCs) based upon either inductive or capacitive metal meshes of different mesh sizes on a crystal quartz substrate to provide different amounts of reflectance [44, 45]. Due to the FP effect of the substrate, the transmittance/reflectance of these OCs changes with frequency in a oscillating manner, which we measured exactly using a FTIR spectrometer (see Appendix). Unlike using a polarizer as OC, these metal mesh OCs are insensitive to polarization. In the

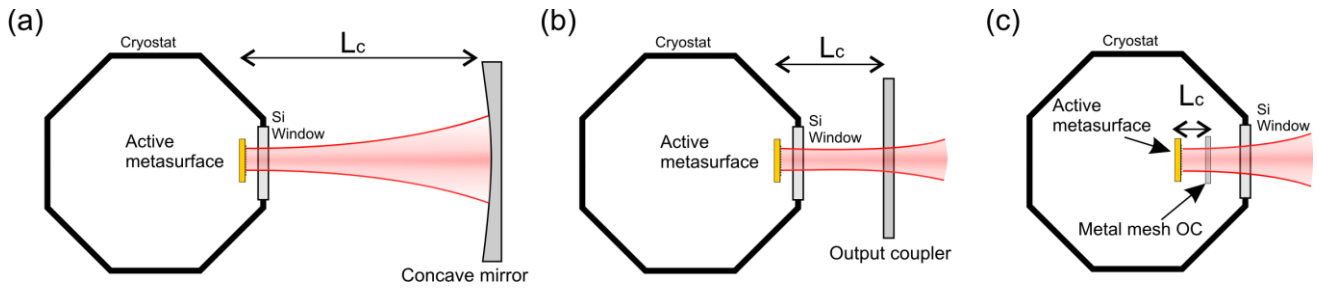

Fig. 7. Schematics of three QC-VECSEL cavity designs: (a) plano-conave mirror Gaussian cavity; (b) plano-plano Fabry-Pérot cavity; (c) plano-plano compact cavity inside a cryostat.

recently demonstrated focusing metasurface QC-VECSEL [46], we used these metal mesh OCs to form a cavity, instead of a wire-grid polarizer, to prevent the polarized response from the OC from interfering with the focusing effect. The QC-VECSEL based on a focusing metasurface exhibits a higher stability than the previous plano-plano FP cavity, resembling a concave-plano hemispherical cavity. This is confirmed by the numerical modeling of cavity loss change with the misaligned angle between OC/concave mirror and metasurface, based on a modified Fox-and-Li method [47], which is shown in Fig. 8 (See Section V for experimental data on focusing metasurface VECSELs).

The third type of QC-VECSEL cavity that we have demonstrated is a compact intra-cryostat cavity, as shown in Fig. 7(c). The parallelism between the OC and metasurface is achieved by fine tuning a specially designed mechanical stage at room temperature, which is then mounted inside the cryostat and cooled down. While this approach prevents fine alignment of the cavity during operation, our experience so far suggests that misalignment during cooldown is not a significant problem for high performance metasurfaces. In particular, using a focusing metasurface and a short cavity length can help to reduce the sensitivity to misalignment in this configuration. This compact cavity is not only convenient for application, but also eliminates any possible loss from the cryostat window and the atmosphere. The lasing threshold for this cavity has been found to be much lower than the external FP cavity counterpart with the same OC and metasurface (see Fig. 13).

V. Experimental Results

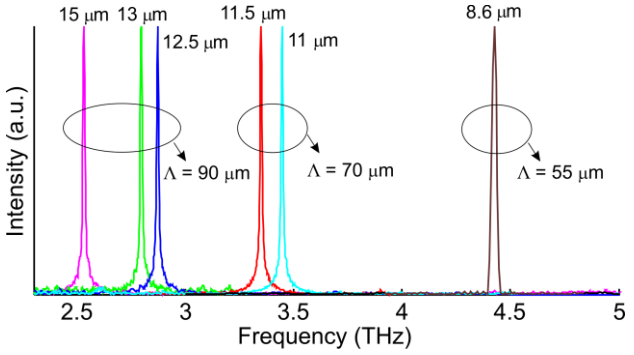

Fig. 9. Measured lasing spectra for some demonstrated QC-VECSELs based on various metasurfaces designed with different ridge widths (labels above each spectrum show the nominal width) and periods Λ fabricated on different active QC-laser materials.

A. Spectral Engineering

So far we have demonstrated various QC-VECSELs lasing in a range from 2.5 – 4.4 THz. This is achieved by designing metasurfaces with different periods Λ and ridge widths *w* and pairing them with various resonant-phonon QC-laser active region designs [4, 30]. Fig. 9 shows a family of lasing spectra from different THz QC-VECSELs, all of which were taken using the OC outside the cryostat (except the 4.4 THz demonstrated with a intra-cryostat cavity). As expected, there is an approximate inverse relationship between ridge width *w* and the lasing frequency. Typically the lasing is in single-mode when the cavity length is optimized to achieve a maximum power output. This is attributed to the frequency dependence of the metasurface gain response, in conjunction with the etalon filter effect of the cryostat window. A ~3-mm thick high-resistivity silicon window is typically used in order to minimize the loss (estimated round-trip loss of 7%) – however the large index of Si creates a strong Fabry-Pérot filtering effect. As the cavity is tuned away from its optimum length, hopping between longitudinal modes separated by the window's free spectral range and lasing in multiple longitudinal modes are occasionally observed. Temperature change can also induce a longitudinal mode hop [29].

B. Metasurface QC-VECSELs paired with different OCs

One advantage of THz QC-VECSEL is the freedom of controlling output coupling efficiency by either turning the polarizer as explained in [29] or simply using different metal mesh OCs. This not only allows the optimum coupling efficiency to be readily achieved, but also provides an approach to study the loss from a passive metasurface, similar to extracting the waveguide guide loss by measuring lasers of various ridge length [48]. For this study, we used four output couplers (labeled as OC-1 to OC-4) fabricated all on one ~100 μm-thick quartz substrate and comprised of either capacitive or inductive metal meshes of different sizes to systematically vary the reflectance R_2. We measured the transmittance T_2 (spectra shown in Appendix) such that that R_2=1– T_2 . Fig. 10(a) shows four power-current-voltage (*P-I-V*) curves for the same metasurface paired with each OC. The metasurface is a uniform design with w = 11.5 μm and Λ = 70 μm. Due to the dependence of the OC's reflectance on frequency, the VECSEL lasing frequencies are slightly different. The slope efficiency *dP/dI* and the threshold current density J_{th} are extracted for each *P-I-V* and fitted with the expressions for slope efficiency and threshold current density based on Eq. (11), (12), and (13). We estimate 18% round-trip loss comprising 7% Si window loss and 11% diffraction loss obtained from Fox-and-Li cavity modeling (for this uniform metasurface-plano FP cavity of 9-mm cavity length), such that T^2 = 0.82. Fig. 10(b) and (c) show the extracted *dP/dI* and the threshold current density $J_{th,}$ with the curve fitting result. Fitting the data yields values of R_1 = 0.62, $\eta_i\eta_u = 0.29$, and J_{leak} = 343 A/cm^2. The measured passive reflection is close to the simulated value of 0.76 at resonance frequency of 3.4 THz. If we assume $\eta_u = 0.65$, this implies that the internal quantum efficiency at 77 K is $\eta_i = 0.45$. These values are relatively insensitive to the estimated value of T^2. The bulk gain increase per injected current density was extracted as $\sigma\tau_{eff}/eL_p$ = 0.64 cm/A. This value was obtained assuming $\xi = 1.63\times10^{-2}$ cm from simulation data as in Sec. II; however there is some uncertainty in ξ if VECSEL is in fact lasing slightly detuned from the metasurface resonance. Direct measurements of the metasurface reflectance and gain will be necessary in the future to directly measure this value.

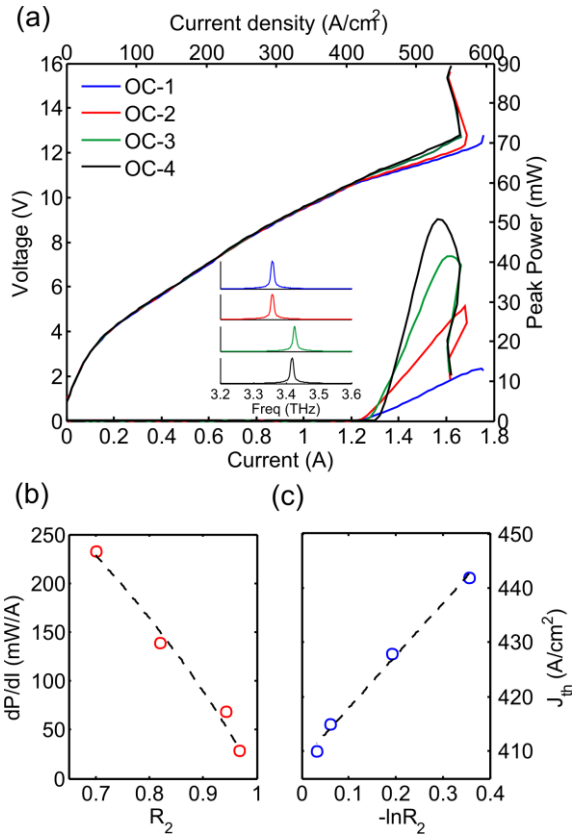

Fig. 10. (a) Measured 77 K pulsed *P-I-V*s for QC-VECSELs built with one metasurface and four OCs. The inset shows the lasing spectra for each VECSEL. (b) Slope efficiency change with the OC reflectance R_2. The black dashed line is the fitted curve. (c) Threshold current density J_{th} change with the OC reflection R_2 represented in $-lnR_2$. The black dashed line is the fitted curve.

C. *Focusing metasurface QC-VECSELs*

Inspired by reflectarray antennas, we demonstrated high-performance THz QC-VECSELs using a focusing metasurface design, which the exhibited a significant improvement in beam pattern and cavity stability [49]. The focusing effect was achieved by spatially modulating the metallic microcavity width to design an inhomogeneous phase response over the metasurface to mimic a concave mirror's phase front [46]. Fig. 11(a) presents the measured *P-I-V* for a QC-VECSEL based on a 2-by-2 mm^2 focusing metasurface designed with an effective curvature radius of R = 20 mm for 3.5 THz. The metal mesh OC is mounted outside the cryostat with a cavity length of ~9 mm and its transmittance is measured to be 0.14 at the lasing frequency. A near-diffraction limited beam pattern with ultra narrow full-width half-maximum (FWHM) beam divergence of 3.4°-by-3.3° [50]. This is among the narrowest beam directly produced by a THz QC-laser reported so far. The measured result agrees with the calculated FWHM divergence of 3.5° for an ideal semispherical Gaussian cavity with a concave mirror of 20 mm curvature radius. The M^2 beam pattern is further measured for the beams generated from some focusing metasurface QC-VECSELs, which gives a low value of M^2 = 1.3 in both x- and y- direction, and leads to a high brightness ($B_r = P/(M_x^2 M_y^2 \lambda^2)$) of 1.86 × 10^6 Wsr^{-1}m^{-2} given a measured output power of P = 27 mW [46, 51]. We also observed a degradation in beam quality with M^2 increased to 2.2 – 2.5 when the cavity length is close to the designed curvature radius for the focusing metasurface, likely as a result of the increased diffraction occurring on the metasurface edge.

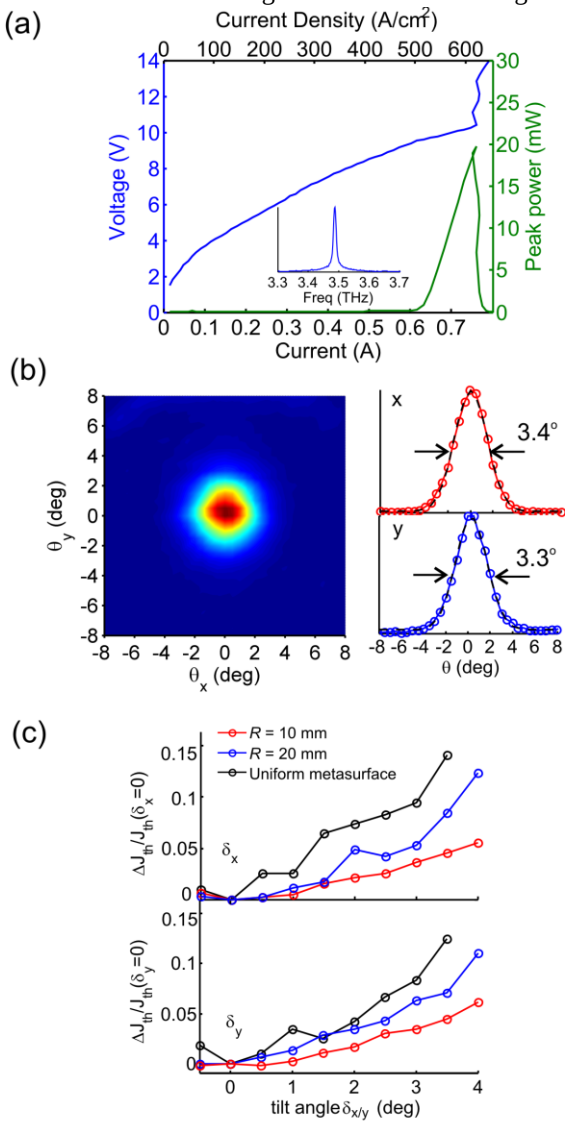

Fig. 11. (a) Measured 77 K pulsed *P-I-V* for a QC-VECSEL based on a R = 20 mm focusing metasurface paired with a metal mesh OC. The set is the lasing spectrum. (b) Measured 2D beam pattern for the focusing metasurface QC-VECSEL and 1D cuts of the beam in x and y direction. Black dashed lines are the Gaussian curve fits. (c) Measured threshold current density change with δ_x and δ_y for QC-VECSELs based upon three different metasurfaces. (Figures originally published in [46]).

The focusing designs were found to be easier to align and more tolerant of misalignment than uniform metasurface designs. The cavity stability improvement is further quantified by first optimizing the alignment of the cavity to achieve parallelism, and then intentionally introducing angular misalignment in either the x or y axis by tilt angles δ_x and δ_y respectively. At each misalignment setting, a *P-I-V* was measured and the threshold current density J_{th} was recorded. We performed this measurement for three metasurfaces: focusing metasurfaces of R = 10 mm and 20 mm, and a uniform metasurface similar to the design in [29]. As shown in Fig. 11(c), J_{th} increases with the tilt angle in both axes in a modest manner for the two focusing metasurface QC-VECSELs – devices still lase even with 4° misalignment. In contrast, the

uniform metasurface exhibits a dramatic rise in J_{th} with misalignment, and ceases to lase for misalignments greater than 3.5°. This effect is particularly notable for longer cavities due to larger walk-off losses. So the focusing design is beneficial for a cavity with OC external to the cryostat, which has a cavity length no less than ~9 mm due to the experimental constraints.

D. Intra-cryostat cavity QC-VECSEL

To further improve the compactness and performance of QC-VECSEL, it is possible to contain the entire cavity within the cryostat, as shown in Fig. 7(c). This avoids any loss and etalon effect associated with the cryostat window and atmosphere. A miniature mount was designed to hold the OC in parallel with the metasurface, which is fine tuned at room temperature and then mounted inside the cryostat. After cooldown, it is possible that thermal contraction may introduce angular misalignment of OC and we lack access to correct it. To mitigate this effect, it is helpful to use short cavity lengths of 2–3 mm in order to keep the cavity loss due to OC misalignment at a low level. Use of a focusing metasurface is also helpful, although not essential, to reduce the effects of misalignment.

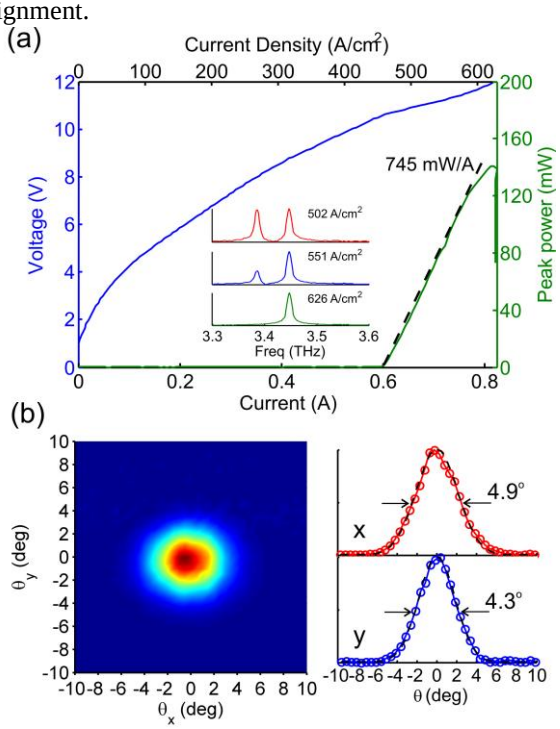

Fig. 12. (a) Measured 77 K pulsed *P-I-V* for an intra-cryostat cavity QC-VECSEL based on a uniform metasurface. paired with a metal mesh OC mounted inside the cryostat. The inset shows the spectra change with the current injection level. (b) Measured 2D beam pattern for the intra-cryostat cavity QC-VECSEL and 1D cuts of the beam in x and y direction. Black dashed lines are the Gaussian curve fits.

Some of the best performing QC-VECSELs to date have been achieved in this configuration. An example is a device with a high peak power of 140 mW in pulsed mode at 77 K, based on a 2-by-2 mm^2 uniform metasurface with 11.5-μm ridge width and 70-μm periodicity, and with a center circular area of 1 mm diameter biased. The slope efficiency is a record high 745 mW/A for a THz QC-laser at 77 K, which corresponds to roughly 0.33 photons emitted per electron per stage above threshold. The peak wall-plug efficiency was 1.5%. The OC used has its transmittance at 18-20% in the lasing frequency range. The measured spectra show lasing in two neighboring longitudinal modes at low biases, which gradually evolves to a dominant high frequency mode with a higher bias due to the Stark effect in quantum wells. At the peak power bias, the lasing is essentially single-mode. The two modes are separated by 61 GHz (measured with a FTIR spectrometer with 7.5 GHz resolution), from which we can infer that the cavity length is 2.5 mm. Accompanied with the high power output is a near-Gaussian circular beam pattern with a FWHM divergence angle of 4.9°-by-4.3°.

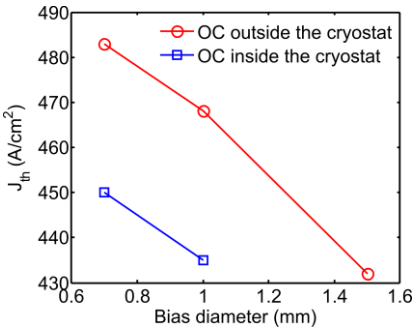

Fig. 13. Measured threshold current densities for focusing metasurface VECSELs based on an identical metasurface design with the only difference in the diameter of the center circular bias area. They are paired with the same OC in two cavity geometries: OC mounted outside and inside the cryostat with cavity length of ~9 mm and 2–3 mm respectively.

We attribute the high power and efficiency performance from this compact cavity QC-VECSEL to the removal of cryostat window loss and air absorption loss, as well as the shortened cavity length that reduces the cavity diffraction loss. This is reflected in the reduced threshold current density as the OC is placed inside the cryostat, as shown in Fig. 13. The loss minimization is also very critical to achieving cw operation at a high temperature (at or above 77 K). In another compact cavity demonstration, we used a focusing metasurface designed with a smaller than usual bias area (circle of 0.7-mm diameter) and observed 83 K cw operation with a considerable amount of power ~5 mW. This is larger than previous records for cw power at 77 K, which are typically 1–2 mW at best in metal-metal waveguides [22, 30, 52]. The only drawback of reducing bias area is the resulting increase in threshold current density shown in Fig. 13, due to the reduced transverse confinement factor Γ_t (see Fig. 6). This high-power cw performance illustrates a further advantage of the metasurface VECSEL approach. The active material is essentially diluted over a large area in sparse ridge microcavities; this decreases the power dissipation density and provides a more favorable geometry for cooling than for a single wider ridge waveguide. Putting aside improvements in the underlying QC-active material, further improvements in cw performance from VECSELs are likely possible by (a) improving heat removal via better heat sinking (no substrate thinning has been performed for the current devices), (b) reducing the bias area to reduce the total drive current, (c) increasing the sparsity of the metasurface (by using patches rather than ridges for example [53, 54]).

VI. Conclusion

We have reviewed the state-of-the-art for THz QC-VECSELs in terms of the metasurface theory and design, laser model for idealized QC-VECSEL, cavity design, frequency engineering, output coupling efficiency analysis, and some recent high-performance achievements. QC-VECSELs have exhibited a significant improvement to THz QC-lasers in many aspects, including a directive, near-diffraction limited beams of 3.4°-by-3.3° FWHM divergence, a high pulsed output power of 140 mW with a high slope efficiency of 745 mW/A at 77 K, and cw operation with ~5 mW power output at 77 K. The QC-VECSEL approach paves a promising way to make high-performance QC-lasers. Higher power output and improved performance at cw or high temperature are projected by scaling up the metasurface area, and optimizing the thermal dissipation efficiency through metasurface design and thermal engineering. Furthermore, advanced metasurface designs enable QC-VECSELs with new functionality such as electrically-switchable polarization [50].

Appendix

A. Output couplers

The measured transmission spectra for the four metal mesh OCs used in Fig. 4 are shown in Fig. 14. Measured transmission spectra for four metal mesh OCs. They are all fabricated on one quartz substrate of ~100-μm thickness.

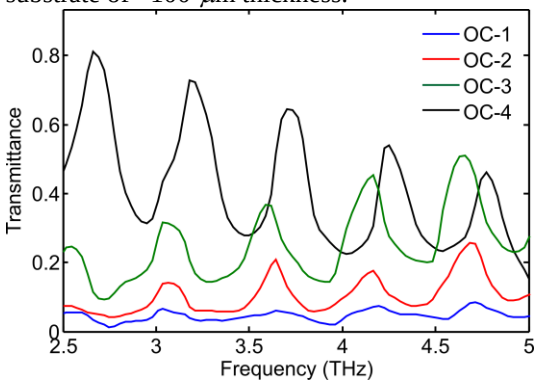

Fig. 14. Measured transmission spectra for four metal mesh OCs.

B. Relationship to conventional formalism

The formalism defined in Sec. III can be linked to a more common form for semiconductor lasers, if one defines the threshold gain g_{th} in terms of a loss coefficient α_{cav} (prorated over the cavity round trip length $2L$) according to:

$$g_{th} = \frac{n}{\Gamma}\alpha_{cav} = -\frac{n}{\Gamma}\frac{\ln\left(T^2 R_1 R_2\right)}{2L}, \tag{14}$$

where $\Gamma = \Gamma_l \Gamma_t$ is a modal confinement factor which describes the overlap of the mode with the QC-active material (satisfying the polarization selection rule). It can be defined using a standard expression,

$$\Gamma = \Gamma_l \Gamma_t = \frac{\int_{\text{act}} \varepsilon(\mathbf{R})\left|E_z(\mathbf{R})\right|^2 dV}{\int_V \varepsilon(\mathbf{R})\left|E(\mathbf{R})\right|^2 dV}, \tag{15}$$

which can be conceptually separated into a longitudinal confinement factor $\Gamma_l(\nu)$ and a transverse confinement factor Γ_t. The longitudinal confinement factor contains the field enhancement effects of the microcavity resonance $M(\nu)$. For large cavity lengths, and using the field in Eq. (6), we can approximate

$$\Gamma_l(\nu) \approx \frac{hn^2 M(\nu) F}{2L(1+R_1 G_{th})}. \tag{16}$$

This expression has undesirable feature that it depends upon the threshold gain G_{th}. However, in the limit of a high finesse cavity, R_1, R_2, T, and G_{th} are all close to unity. In this limiting case, Γ_l is directly proportional to the fitted ξ parameter extracted from the numerical metasurface simulation: $\xi = 2L\Gamma_l / n$ (see Eq. (1)).

When the transverse extent of the mode is smaller than the biased area of the metasurface, the transverse confinement factor Γ_t is unity (see Fig. 6 for the dependence of Γ_t on the filling of a metasurface with different mode sizes). However, for cases where only a section of the metasurface receives current injection over a "bias area," we can use

$$\Gamma_t = \frac{\int_{\text{bias area}} \left|\psi(x,y)\right|^2 dA}{\int \left|\psi(x,y)\right|^2 dA}, \tag{17}$$

Note, if we assume a lossless transmittance for the external cavity, i.e. $T = 1$, the optical coupling efficiency in Eq. (11) reduces to $\eta_{opt} = \alpha_m / \alpha_{cav}$ where $\alpha_m = -\ln R_2 / 2L$ is the prorated output mirror loss coefficient. The threshold current density becomes

$$J_{th} = \frac{eL_p}{\sigma\tau_{eff}}\frac{n}{\Gamma}\alpha_{cav} + J_{leak}, \tag{18}$$

These are the classic formulas for J_{th} and dP/dI for waveguide based QC-lasers. The factor of n in these definition results from the fact that the prorated loss coefficients are over a length $2L$ in vacuum, while the gain coefficient is defined in the semiconductor medium with refractive index n.

References

[1] R. Köhler, A. Tredicucci, F. Beltram, H. E. Beere, E. H. Linfield, A. G. Davies, D. A. Ritchie, R. C. Iotti, and F. Rossi, "Terahertz semiconductor-heterostructure laser," *Nature*, vol. 417, p. 156, 2002.

[2] B. S. Williams, "Terahertz quantum cascade lasers," *Nat. Photon.*, vol. 1, pp. 517-524, 2007.

[3] M. S. Vitiello, G. Scalari, B. Williams, and P. De Natale, "Quantum cascade lasers: 20 years of challenges," *Opt. Express*, vol. 23, pp. 5167-5182, 2015.

[4] L. Li, L. Chen, J. Zhu, J. Freeman, P. Dean, A. Valavanis, A. G. Davies, and E. H. Linfield, "Terahertz quantum cascade lasers with >1 W output powers," *Electron. Lett.*, vol. 50, pp. 309-311, 2014.

[5] Y.-Y. Li, J.-Q. Liu, F.-Q. Liu, J.-C. Zhang, S.-Q. Zhai, N. Zhuo, L.-J. Wang, S.-M. Liu, and Z.-G. Wang, "High power-efficiency terahertz quantum cascade laser," *Chinese Physics B*, vol. 25, p. 084206, 2016.

[6] L. Li, I. Kundu, P. Dean, E. H. Linfield, and A. G. Davies, "High-power GaAs/AlGaAs quantum cascade lasers with emission in the frequency range 4.7–5.6 THz," in *International Quantum Cascade Lasers School and Workshop*, Cambridge, UK, 2016.

[7] S. Fathololoumi, E. Dupont, C. W. I. Chan, Z. R. Wasilewski, S. R. Laframboise, D. Ban, A. Mátyás, C. Jirauschek, Q. Hu, and H. C. Liu, "Terahertz quantum cascade lasers operating up to ~200 K with

optimized oscillator strength and improved injection tunneling," *Opt. Express*, vol. 20, pp. 3866-3876, 2012.

[8] M. Wienold, B. Röben, L. Schrottke, R. Sharma, A. Tahraoui, K. Biermann, and H. T. Grahn, "High-temperature, continuous-wave operation of terahertz quantum-cascade lasers with metal-metal waveguides and third-order distributed feedback," *Opt. Express*, vol. 22, pp. 3334-3348, 2014.

[9] J. R. Gao, J. N. Hovenier, Z. Q. Yang, J. J. A. Baselmans, A. Baryshev, M. Hajenius, T. M. Klapwijk, A. J. L. Adam, T. O. Klaassen, B. S. Williams, S. Kumar, Q. Hu, and J. L. Reno, "A terahertz heterodyne receiver based on a quantum cascade laser and a superconducting bolometer," *Appl. Phys. Lett.*, vol. 86, p. 244104, 2005.

[10] H. Richter, M. Wienold, L. Schrottke, K. Biermann, H. T. Grahn, and H.-w. Hübers, "4.7-THz Local Oscillator for the GREAT Heterodyne Spectrometer on SOFIA," *IEEE Trans. THz Sci. Technol.*, vol. 5, pp. 539-545, 2015.

[11] C. Walker, C. Kulesa, J. Kloosterman, D. Lesser, T. Cottam, C. Groppi, J. Zmuidzinas, M. Edgar, S. Radford, P. Goldsmith, W. Langer, H. Yorke, J. Kawamura, I. Mehdi, D. Hollenbach, J. Stutzski, H. Huebers, J. R. Gao, and C. Martin, "Large Format HeterodyneArrays for Observing Far-Infrared Lines with SOFIA " *Proc. SPIE*, vol. 7741, p. 77410Z, 2010.

[12] A. W. M. Lee, Q. Qin, S. Kumar, B. S. Williams, Q. Hu, and J. L. Reno, "Real-time terahertz imaging over a standoff distance (>25 meters)," *Appl. Phys. Lett.*, vol. 89, p. 141125, 2006.

[13] V. P. Wallace, A. J. Fitzgerald, S. Shankar, R. J. Pye, and D. D. Arnone, "Terahertz pulsed imaging of basal cell carcinoma ex vivo and in vivo," *Br. J. Dermatol.*, vol. 151, pp. 424–432, 2004.

[14] S. M. Kim, F. Hatami, J. S. Harris, A. W. Kurian, J. Ford, D. King, G. Scalari, M. Giovannini, N. Hoyler, J. Faist, and G. Harris, "Biomedical terahertz imaging with a quantum cascade laser," *Appl. Phys. Lett.*, vol. 88, p. 153903, 2006.

[15] Y. L. Hor, J. F. Federici, and R. L. Wample, "Nondestructive evaluation of cork enclosures using terahertz/millimeter wave spectroscopy and imaging," *Appl. Opt.*, vol. 47, pp. 72-78, 2008.

[16] C. Stoik, M. Bohn, and J. Blackshire, "Nondestructive evaluation of aircraft composites using reflective terahertz time domain spectroscopy," *Ndt & E International*, vol. 43, pp. 106-115, 2010.

[17] A. J. L. Adam, I. Kašalynas, J. N. Hovenier, T. O. Klaassen, J. R. Gao, E. E. Orlova, B. S. Williams, S. Kumar, Q. Hu, and J. L. Reno, "Beam patterns of terahertz quantum cascade lasers with subwavelength cavity dimensions," *Appl. Phys. Lett.*, vol. 88, p. 151105, 2006.

[18] A. W. M. Lee, Q. Qin, S. Kumar, B. S. Williams, Q. Hu, and J. L. Reno, "High-power and high-temperature THz quantum-cascade lasers based on lens-coupled metal-metal waveguides," *Opt. Lett.*, vol. 32, pp. 2840-2842, 2007.

[19] M. I. Amanti, M. Fischer, G. Scalari, M. Beck, and J. Faist, "Low-divergence single-mode terahertz quantum cascade laser," *Nat. Photon.*, vol. 3, pp. 586-590, 2009.

[20] T.-Y. Kao, Q. Hu, and J. L. Reno, "Perfectly phase-matched third-order distributed feedback terahertz quantum-cascade lasers," *Opt. Lett.*, vol. 37, pp. 2070-2072, 2012.

[21] T.-Y. Kao, Q. Hu, and J. L. Reno, "Phase-locked arrays of surface-emitting terahertz quantum-cascade lasers," *Appl. Phys. Lett.*, vol. 96, p. 101106, 2010.

[22] G. Xu, R. Colombelli, S. P. Khanna, A. Belarouci, X. Letartre, L. Li, E. H. Linfield, A. G. Davies, H. E. Beere, and D. A. Ritchie, "Efficient power extraction in surface-emitting semiconductor lasers using graded photonic heterostructures," *Nat. Commun.*, vol. 3, p. 952, 2012.

[23] Y. Chassagneux, R. Colombelli, W. Maineult, S. Barbieri, H. E. Beere, D. A. Ritchie, S. P. Khanna, E. H. Linfield, and A. G. Davies, "Electrically pumped photonic-crystal terahertz lasers controlled by boundary conditions," *Nature*, vol. 457, pp. 174-178, 2009.

[24] T. Y. Kao, J. L. Reno, and Q. Hu, "Phase-locked laser arrays through global antenna mutual coupling," *Nat. Photon.*, vol. 10, pp. 541-546, 2016.

[25] C. Wu, S. Khanal, J. L. Reno, and S. Kumar, "Terahertz plasmonic laser radiating in an ultra-narrow beam," *Optica*, vol. 3, pp. 734-740, 2016.

[26] A. C. Tropper, H. D. Foreman, A. Garnache, K. G. Wilcox, and S. H. Hoogland, "Vertical-external-cavity semiconductor lasers," *J. Phys. D: Appl. Phys.*, vol. 37, pp. R75-R85, 2004.

[27] M. Kuznetsov, F. Hakimi, R. Sprague, and A. Mooradian, "High-Power (0.5-W CW) Diode-Pumped Vertical-External-Cavity Surface-Emitting Semiconductor Lasers with Circular TEM Beams," *IEEE Photon. Tech. Lett.*, vol. 9, pp. 1063-1065, 1997.

[28] B. Rudin, A. Rutz, M. Hoffmann, D. J. H. C. Maas, A.-R. Bellancourt, E. Gini, T. Südmeyer, and U. Keller, "Highly efficient optically pumped vertical-emitting semiconductor laser with more than 20 W average output power in a fundamental transverse mode," *Opt. Lett.*, vol. 33, pp. 2719-2721, 2008.

[29] L. Xu, C. A. Curwen, P. W. C. Hon, Q.-S. Chen, T. Itoh, and B. S. Williams, "Metasurface external cavity laser," *Appl. Phys. Lett.*, vol. 107, p. 221105, 2015.

[30] B. S. Williams, S. Kumar, Q. Hu, and J. L. Reno, "Operation of terahertz quantum-cascade lasers at 164 K in pulsed mode and at 117 K in continuous-wave mode," *Opt. Express*, vol. 13, p. 3331, 2005.

[31] P. W. C. Hon, Z. Liu, T. Itoh, and B. S. Williams, "Leaky and bound modes in terahertz metasurfaces made of transmission-line metamaterials," *J. Appl. Phys.*, vol. 113, p. 033105, 2013.

[32] P. W. C. Hon, A. A. Tavallaee, Q.-S. Chen, B. S. Williams, and T. Itoh, "Radiation Model for Terahertz Transmission-Line Metamaterial Quantum-Cascade Lasers," *IEEE Trans. Terahertz Science and Technology* vol. 2, pp. 323-332, 2012.

[33] A. A. Tavallaee, B. S. Williams, P. W. C. Hon, T. Itoh, and Q.-S. Chen, "Terahertz quantum-cascade laser with active leaky-wave antenna," *Appl. Phys. Lett.*, vol. 99, p. 141115, 2011.

[34] Y. Todorov, L. Tosetto, J. Teissier, A. M. Andrews, P. Klang, R. Colombelli, I. Sagnes, G. Strasser, and C. Sirtori, "Optical properties of metal-dielectric-metal microcavities in the THz frequency range," *Opt. Express*, vol. 18, pp. 13886-13907, 2010.

[35] N. Laman and D. Grischkowsky, "Terahertz conductivity of thin metal films," *Appl. Phys. Lett.*, vol. 93, p. 051105, 2008.

[36] W. J. Moore and R. T. Holm, "Infrared dielectric constant of gallium arsenide," *J. Appl. Phys.*, vol. 80, p. 6939, 1996.

[37] P. Jouy, Y. Todorov, A. Vasanelli, R. Colombelli, I. Sagnes, and C. Sirtori, "Coupling of a surface plasmon with localized subwavelength microcavity modes," *Appl. Phys. Lett.*, vol. 98, 2011.

[38] M. Malerba, T. Ongarello, B. Paulillo, J. M. Manceau, G. Beaudoin, I. Sagnes, F. De Angelis, and R. Colombelli, "Towards strong light-matter coupling at the single-resonator level with sub-wavelength mid-infrared nano-antennas," *Appl. Phys. Lett.*, vol. 109, 2016.

[39] A. Liu, W. Hofmann, and D. Bimberg, "Two dimensional analysis of finite size high-contrast gratings for applications in VCSELs," *Opt. Express*, vol. 22, pp. 11804-11811, 2014.

[40] B. S. Williams, "Terahertz quantum cascade laser," Ph.D., Electrical Engineering and Computer Science, Massachusetts Institute of Technology, 2003.

[41] J. Faist, "Wallplug efficiency of quantum cascade lasers: Critical parameters and fundamental limits," *Appl. Phys. Lett.*, vol. 90, p. 253512, 2007.

[42] T. Gresch, M. Giovannini, N. Hoyer, and J. Faist, "Quantum cascade lasers with large optical waveguides," *IEEE Photon. Tech. Lett.*, vol. 18, pp. 544-546, 2006.

[43] L. Xu, P. Hon, T. Itoh, and B. S. Williams, "Terahertz quantum cascade metasurface external cavity laser," presented at the Intersubband Transitions in Quantum Wells (ITQW) 2015, Vienna, Austria, 2015.

[44] R. Densing, A. Erstling, M. Gogolbwski, H.-P. Gemund, G. Lundershausen, and A. Gatesman, "Effective far infrared laser operation with mesh couplers," *Infrared Phys.*, vol. 33, pp. 219-226, 1992.

[45] S. T. Shanahan and N. R. Heckenberg, "Transmission line model of substrate effects on capacitive mesh couplers," *Appl. Opt.*, vol. 20, pp. 4019-4023, 1981.

[46] L. Xu, D. Chen, T. Itoh, J. L. Reno, and B. S. Williams, "Focusing metasurface quantum-cascade laser with a near diffraction-limited beam," *Opt. Express*, vol. 24, pp. 24117-24128, 2016.

[47] A. G. Fox and T. Li, "Resonant Modes in a Maser Interferometer," *Bell Systems Technical Journal*, vol. 40, pp. 453-488, 1961.

[48] M. Razeghi, "High-Performance InP-Based Mid-IR Quantum Cascade Lasers," *IEEE J. Sel. Topics Quantum Electron.*, vol. 15, pp. 941-951, 2009.

[49] D. M. Pozar, S. D. Targonski, and H. D. Syrigos, "Design of Millimeter Wave Microstrip Reflectarrays," *IEEE Trans. Antennas and Propagat.*, vol. 45, pp. 287-296, 1997.
[50] L. Xu, D. Chen, C. A. Curwen, M. Memarian, J. L. Reno, T. Itoh, and B. S. Williams, "Metasurface quantum-cascade laser with electrically-switchable polarization," *Optica*, 2017 (In press).
[51] "International Organization for Standardization, document no. ISO 11146, Lasers and laser-related equipment – Test methods for laser beam parameters – Beam width, divergence, angle and beam propagation factor," ed, 1999.
[52] M. I. Amanti, G. Scalari, F. Castellano, M. Beck, and J. Faist, "Low divergence Terahertz photonic-wire laser," *Opt. Express*, vol. 18, pp. 6390-6395, 2010.
[53] C. Feuillet-Palma, Y. Todorov, A. Vasanelli, and C. Sirtori, "Strong near field enhancement in THz nano-antenna arrays," *Sci. Rep.*, vol. 3, 2013.
[54] D. Palaferri, Y. Todorov, Y. N. Chen, J. Madeo, A. Vasanelli, L. H. Li, A. G. Davies, E. H. Linfield, and C. Sirtori, "Patch antenna terahertz photodetectors," *Appl. Phys. Lett.*, vol. 106, 2015.

Luyao Xu is expecting to obtain her Ph.D. degree in Electrical Engineering from UCLA in June 2017. She received her Master's degree in 2013 from Electrical Engineering Dept. at UCLA, and her Bachelor's Degree in Optical Engineering in Zhejiang University, China in 2011. Her Ph.D. research is focused on investigating terahertz (THz) metasurface quantum cascade (QC) lasers, i.e. THz metasurface QC-VECSEL, to achieve high power in combination with an excellent beam pattern. She is also exploring the novel metasurface design to develop new functionalities for QC-laser. Her research interests span photonic meta-structures, cavity engineering and quantum cascade devices. Ms. Xu has received awards including UCLA PhD Dissertation Year Fellowship, Best Student Presentation Award in SPIE Photonics West 2016 (VECSEL sub-conference session), SPIE Optics and Photonics Scholarship, First Place Award in UCLA E.E. PhD Preliminary Exam Excellent Award, UCLA Departmental Graduate Student Fellowship.

Christopher A. Curwen received his B.S. in Electrical Engineering from Penn State in 2012 and is currently working towards his Ph.D. in Electrical Engineering at UCLA. His research interests include engineering electromagnetics, metamaterials, and laser physics.

Daguan Chen is expecting to receive his B.S. in electrical engineering from the University of California, Los Angeles in June 2017. From 2015 to 2017 he was an Undergraduate Researcher in the Terahertz Devices and Intersubband Nanostructures Laboratory at UCLA, where he researched terahertz-active metasurface lasers.

John Reno is an internationally recognized expert on Molecular Beam Epitaxy (MBE) growth. He is part of the Center for Integrated Nanotechnologies (CINT) at Sandia National Laboratories. John's primary research interests presently are in the area of high-purity nanostructured electronic materials, with an emphasis on the synthesis of AlGaInAs based materials. Current research interests focus on intersubband transitions and high mobility heterostructures. Research includes quantum cascade lasers in the THz and IR range, quantum well infrared photodetectors (QWIP), high mobility materials for low-dimensional quantum transport studies, and the study of the interaction between semiconductor materials and metamaterial for new optical applications. Prior to his present work, he has performed MBE growth of a wide range of materials including HgCdTe, wide gap II-VI materials, high T_c superconductors, narrow gap group IV materials, and short period superlattices on InP.

Tatsuo Itoh received the Ph.D. Degree in Electrical Engineering from the University of Illinois, Urbana in 1969. After working for University of Illinois, SRI and University of Kentucky, he joined the faculty at The University of Texas at Austin in 1978, where he became a Professor of Electrical Engineering in 1981. In September 1983, he was selected to hold the Hayden Head Centennial Professorship of Engineering at The University of Texas. In January 1991, he joined the University of California, Los Angeles as Professor of Electrical Engineering and holder of the TRW Endowed Chair in Microwave and Millimeter Wave Electronics (currently Northrop Grumman Endowed Chair). He received a number of awards including IEEE Third Millennium Medal in 2000, and IEEE MTT Distinguished Educator Award in 2000. He was elected to a member of National Academy of Engineering in 2003. Dr. Itoh is a Fellow of the IEEE, a member of the Institute of Electronics and Communication Engineers of Japan, and Commissions B and D of USNC/URSI. He served as the Editor of IEEE Transactions on Microwave Theory and Techniques for 1983-1985. He was President of the Microwave Theory and Techniques Society in 1990. He was the Editor-in-Chief of IEEE Microwave and Guided Wave Letters from 1991 through 1994. He was elected as an Honorary Life Member of MTT Society in 1994. He was the Chairman of Commission D of International URSI for 1993-1996. He serves on advisory boards and committees of a number of organizations. He served as Distinguished Microwave Lecturer on Microwave Applications of Metamaterial Structures of IEEE MTT-S for 2004 - 2006. He has 375 journal publications, 775 refereed conference presentations and has written 43 books/book chapters in the area of microwaves, millimeter waves, antennas and numerical electromagnetics. He generated 70 Ph.D. students.

Benjamin S. Williams received the Ph.D. degree from the Massachusetts Institute of Technology, Cambridge, Massachusetts in 2003 in Electrical Engineering and Computer Science. He was a Postdoctoral Associate at the Research Laboratory of Electronics at MIT from 2003-2006. In 2007, he joined the Electrical Engineering Department at the University of California, Los Angeles, where he is currently Associate Professor and a Henry Samueli Fellow. His research interests include quantum cascade lasers, intersubband and intersublevel devices in semiconductor nanostructures, and terahertz metamaterials and plasmonics. He is currently an Associate Editor of IEEE Journal of Quantum Electronics, and on the Editorial Board of IEEE Transactions in Terahertz Science and Technology. Prof. Williams has received awards including the Apker Award from the American Physical Society, the Young Investigator Award from the Defense Advanced Research Projects Agency (DARPA), the Early Career Award from the National Science Foundation (NSF CAREER), and the Presidential Early Career Award for Scientists and Engineers (PECASE).